



Dislocation loops, segregation and hardening induced by high-dose ion irradiation of NbMoTaW and VCrTaW high-entropy alloy coatings on the T91 substrate

Hongtai Luo ^a, Bin Long ^{b,*}, Shenghui Lu ^b, Liping Guo ^{a,*}, Fengfeng Luo ^c, Wenbin Lin ^a, Junjie Cao ^a, Zepeng Yin ^a, Peili Zhao ^d

^a Hubei Nuclear Solid Physics Key Laboratory, Key Laboratory of Artificial Micro- and Nano-Structures of Ministry of Education and School of Physics and Technology, Wuhan University, Wuhan 430072, China

^b China Institute of Atom Energy, Beijing 102413, China

^c Software Engineering Institute of Guangzhou, Guangzhou 510990, China

^d School of Physics and Technology, Center for Electron Microscopy, Wuhan University, Wuhan 430072, China



ARTICLE INFO

Keywords:

High-entropy alloy coatings

Ion irradiation

Segregation

Dislocation loops

Hardening

ABSTRACT

NbMoTaW and VCrTaW high-entropy alloys (HEA) coatings with near-equal atomic ratios were deposited onto the T91 substrate by magnetron sputtering. The two HEA coatings and the T91 substrate were irradiated to the peak damage 50 displacements per atom (dpa) and 100 dpa using 2.7 MeV Si²⁺ at 550 °C. X-ray diffraction (XRD), Scanning electron microscopy (SEM), transmission electron microscopy (TEM), energy dispersive X-ray spectroscopy (EDS) and nanoindentation techniques were used to study the changes in grain morphology, microstructure, element distribution and hardness before and after irradiation. The results showed that the grain structure was stable and the coatings were closely bonded to the substrate after irradiation. The elements (Ta and W) near the grain boundary in NbMoTaW coating were depleted before irradiation, but they became homogenized after irradiation. A large number of dislocation loops were observed in both the T91 substrate and HEA coatings after irradiation, the HEA coatings significantly increased the doses required for the full evolution of the dislocation loops. With the increase of damage doses, the dislocation loops size of HEA coatings increased and the number density decreased. The size of the dislocation loops of the two coatings was similar, while the number density of the dislocation loops of NbMoTaW coating was lower than that of VCrTaW coating. Both HEA coatings were significantly hardened after irradiation and the hardening rate of NbMoTaW coating was lower than that of VCrTaW coating. Interestingly, the hardening rate of 50 dpa was higher than 100 dpa for both HEA coatings, which was determined by softening factor and hardening factor in the irradiation process. Based on the defects and hardening rate caused by irradiation, it was preliminarily concluded that NbMoTaW coating had better irradiation resistance, and the above results provide an important reference for the subsequent optimization of lead-based fast reactors structural materials.

1. Introduction

Lead or lead-based alloys (e.g. lead-bismuth alloys) have high waste transmutation and nuclear fuel proliferation capability due to their weak absorption and moderation ability for neutrons [1]. At the same time, lead-based alloys have a low melting point, high boiling point, strong heat-carrying capacity, and weak chemical reactivity with air and water, making lead-based fast reactors have higher thermal efficiency and safety, and become mature fourth-generation reactor candidates [2,3].

However, because the operating environment of the lead-based fast reactors has a high temperature, severe irradiation, high thermal stress, and the strong corrosion of lead-bismuth liquid metal to structural materials, more stringent requirements are put forward for structural materials [4,5]. At present, there are two main types of structural materials and fuel cladding materials, ferritic/martensitic steel (F/M steel, such as T91, HT9) and austenitic stainless steel (Such as 316 L, 15-15Ti), but they all had liquid metal corrosion problems [6–8]. Early studies suggested that the oxide layer produced by corrosion could protect the

* Corresponding authors.

E-mail addresses: binlong@ciae.ac.cn (B. Long), guolp@whu.edu.cn (L. Guo).

matrix from further oxidation, but this depended on the right oxygen concentration as well as a low corrosion temperature (less than 500 °C) [9–11]. However, the maximum operating temperature of lead-based fast reactors generally exceeds 550 °C [12,13]. Experiments on the European lead-based fast reactors (ELSY) showed that oxygen levels were controlled at 10^{-6} wt% at 550 °C, T91 after the corrosion time in pure lead lasted for 10,000 h, an oxide layer greater than 30 μm thick was formed, and the oxide layer ruptured and lost its protective effect on the matrix [14]. Similarly, Tian et al. [6] controlled the oxygen content at $1\text{--}3 \times 10^{-6}$ wt% at 500 °C, T91 exposed to lead-bismuth alloys for up to 5000 h produces a corrosive oxide layer up to 33 μm, and the local oxide layer was peeled off and further oxidation.

As important as the corrosion of high-temperature lead-bismuth was that the whole life cycle of lead-bismuth fast reactor structural materials and cladding materials was subject to irradiation damage of more than 50–100 dpa, and various microscopic defects such as dislocation loops and cavities generated by irradiation will also aggravate corrosion instability [15]. Searching for structural materials that are more resistant to irradiation and corrosion becomes the key to the development of lead-bismuth reactors.

The HEAs have attracted a lot of attention in recent years, and a HEA in a broad sense refers to more than four alloy components, each with an atomic ratio between 5 at.% - 35 at.% [16,17]. The HEAs have four core effects: high entropy, sluggish diffusion, severe lattice distortion, and cocktail effects [18], these effects result in HEAs with excellent high-temperature mechanical properties [19], irradiation damage resistance [20], and high-temperature corrosion resistance [21,22]. El-Atwani et al. [23] used 1 MeV heavy ions (Kr^+) to irradiate WTaVCr at 800 °C with a dose rate of 1.6×10^{-3} dpa/s and a dose of 8 dpa, and no dislocation loop was observed. Zheng et al. [24] irradiated T91 using 1 MeV Kr^+ ions at 470 °C with a dose rate of $1.07 \pm 0.1 \times 10^{-3}$ dpa/s and a dose of 8 dpa, the size of the dislocation loops was observed to reach 10 nm. It could be seen that the HEA had excellent radiation resistance, but the HEA was not all perfect, due to the complexity of the elements and the melting point gap between elements, segregation will occur during the melt solidification and cooling process, resulting in various casting defects, such as cracks, pores, residual stress, etc. Preparing HEAs in large quantities is a challenge [25].

The corrosion problem of structural materials mainly occurred on the side in contact with the liquid lead-bismuth alloy. Interface engineering could combine the mature process of F/M steel with the irradiation resistance and high-temperature corrosion resistance of HEAs. Yang et al. [26] deposited AlCrFeMoTi on the F/M steel substrate, which showed better corrosion resistance. La et al. [27] deposited WTaVCr coatings with various atomic ratios on the tungsten (W) substrate, which improved the hardness, wear resistance and oxidation resistance.

Considering the high-temperature stability [28], low activation [29], and corrosion resistance [30], the refractory high entropy alloy composed of group VB (V, Nb, Ta) and VIB (Cr, Mo, W) transition metal elements were worth paying attention to, and first-principles calculations showed that the alloying of group V and VI elements could make ductile materials [31]. The first refractory high entropy alloy, NbMoTaW, was prepared by Senkov et al. [32] in 2010 and showed excellent corrosion resistance and high-temperature stability. In addition, the VCrTaW system might exhibit good performance since V and Cr are typical low-activation elements, and the addition of Cr could form a Cr_2O_3 oxide layer, which might improve the corrosion resistance [27]. So, this work chose to deposit NbMoTaW and VCrTaW HEA coatings by a magnetron sputtering method on the T91 substrate. Then, 2.7 MeV Si^{2+} ions were used to irradiate the T91 substrate and HEA coatings at 550 °C reach the peak damage doses of 50 dpa and 100 dpa. The microstructure and mechanical properties of the two kinds of HEA coatings were evaluated after irradiation.

2. Materials and methods

2.1. Material preparation

T91 was prepared by vacuum induction melting at the Shenyang Institute of Metal Research, Chinese Academy of Sciences [33], its chemical composition was shown in Table 1. The HEA coatings were deposited using the ACS-4000 magnetron sputtering ion plating equipment produced by Aifaco Vacuum Technology Co. Ltd. (ULVAC) of Japan. The device had four target positions (two DC and two AC), and the sputtering targets were high-purity Ta, W, V, Cr, Nb and Mo (its purity was higher than 99.99 wt%). Before depositing the HEA coatings, the surface of T91 was polished (consistent with the preparation method of the T91 irradiated sample), the specific treatment method was:

- (1) Rough polished: used 400#, 600#, 1000#, 1600#, and 2000# SiC sandpaper for mechanical polishing until the surface was free of rough scratches.
- (2) Fine polished: used 0.5 μm diamond polishing liquid to assist in mechanical polishing until the grinding surface was bright and scratch-free.

After polishing, the samples were strictly cleaned, that was, ultrasonically cleaned in acetone solution and absolute ethanol for 15 min, and then put into an electric drying oven for rapid drying to prepare for the next deposition. Before deposition, the substrate material was subjected to 10 min of argon ion bombardment cleaning to remove contaminants from the substrate surface. The specific deposition parameters were: the vacuum floor of the sputtering cavity was better than 1×10^{-4} Pa, the flow rate of high-purity argon (99.99 %) was set to 60 sccm, the substrate rotation speed was set to $15 \text{ r}\cdot\text{min}^{-1}$, and the air pressure of the cavity during the deposition process was 0.5 Pa. After sputtering, the samples were fully cooled to room temperature, and the chemical composition of the final HEA coatings measured by EDS was shown in Table 1.

2.2. Ion irradiation

The ion irradiation experiment was completed on the 2×1.7 MV tandem accelerator (GIC4117, General Ionex, America) of the School of Physical Science and Technology, Wuhan University [34]. The displacement damage profile was calculated using Stopping and Range of Ions in Matter (SRIM) 2013 with the “Quick Calculation of Damage Mode”, the displacement energy of Nb, Mo, Ta, W, V, and Cr was 60 eV, 60 eV, 90 eV, 90 eV, 40 eV and 40 eV [35]. The density values used in the simulation were 8.448×10^{22} atoms/cm³ for T91, 5.942×10^{22} atoms/cm³ for NbMoTaW and 6.322×10^{22} atoms/cm³ for VCrTaW. The distribution of displacement damage was shown in Fig. 1, and when the peak damage was 100 dpa, the corresponding ions fluxes of T91, NbMoTaW, and VCrTaW were 2.07×10^{17} ions/cm², 2.71×10^{17} ions/cm² and 2.46×10^{17} ions/cm², respectively. The thermocouple thermometer was close to the samples for temperature measurement, and the temperature was controlled at $550 \text{ }^\circ\text{C} \pm 5 \text{ }^\circ\text{C}$ throughout irradiation, the vacuum degree was maintained at better than 2×10^{-4} Pa.

2.3. Microstructure characterization

Crystalline structures before irradiation were analyzed by X-ray diffraction (XRD-D/MAX 2400, Rigaku, Japan) with Cu K α radiation ($\lambda = 1.5406 \text{ \AA}$) at 40 kV, 40 mA. The surface topography of the samples before and after irradiation was observed by SEM (MIRA3, TESCAN, Czech Republic) of the School of Power and Mechanical Engineering of Wuhan University, and the accelerating voltage was 20 kV, and the SEM equipped with EDS-mapping function, which could perform composition surface scanning analysis of the samples.

The TEM samples were prepared by lift-out method on the focused

Table 1

Chemical composition of T91 and two HEA coatings (at.%).

Sample	Nb	Mo	Ta	W	V	Cr	Si	Mn	C	N	Fe
T91	0.05	0.54	–	–	0.21	9.49	0.94	0.53	0.41	0.16	Bal.
NbMoTaW	21.24	23.05	27.72	27.99	–	–	–	–	–	–	–
VCrTaW	–	–	27.99	28.48	22.14	21.39	–	–	–	–	–

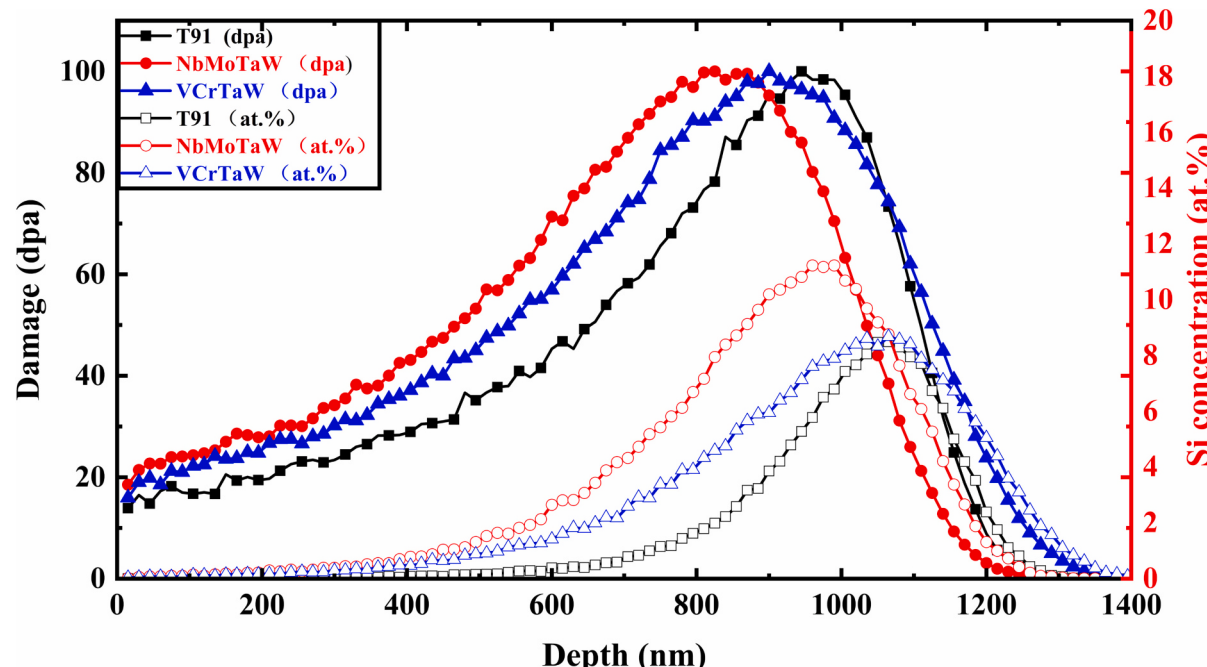


Fig. 1. The displacement damage 100 dpa distribution caused by 2.7 MeV and Si^{2+} simulated by SRIM 2013, and the ions fluxes corresponding to T91, NbMoTaW and VCrTaW were 2.07×10^{17} ions/ cm^2 , 2.71×10^{17} ions/ cm^2 , 2.46×10^{17} ions/ cm^2 .

ion beam (FIB) microscopy (Scios 2 DualBeam, Thermo Scientific, Czech Republic) at the Kaipile Electron Microanalysis Center of Changsha, and the samples were initially thinned to 150 nm by 30 keV Ga^+ ions. Using 5 keV and 2 keV Ga^+ ions further thinned to 100 nm (T91), 50 nm (NbMoTaW and VCrTaW coatings), and low-energy Ga^+ ions could effectively reduce the defects caused by damage of high-energy Ga^+ ions [36]. The microstructure of the irradiated samples was observed on the TEM (Tecani F30, Tecani F30, America) with an electron accelerating voltage of 300 kV at this center. To avoid the influence of bright-field diffraction contrast images on the size of dislocation loops, the average size of the dislocation loops of all samples was calculated under the same g condition. The analysis of elements near grain boundaries in the irradiated and unirradiated regions was performed under the JEOL JEM-NEOARM transmission electron microscope of the electron microscopy center of the School of Physical Science and Technology, Wuhan University, which operated at a voltage of 200 kV.

2.4. Nanoindentation test

The hardness analysis of the samples before and after irradiation was carried out using the nanoindentation instrument (G200*, Agilent Company, America) of the School of Physical Science and Technology, Wuhan University, and the Berkovich indenter was a triangular pyramid. All samples were subjected to the Continuous Stiffness Measurement (CSM) mode to obtain the hardness curve with indentation depth, the test temperature was room temperature, the Strain Rate was 0.05 s^{-1} , the Frequency was 45 Hz, the indentation depth range was 0–1500 nm, the distance between pressure points was greater than 50 μm to exclude the influence between pressure points, and each sample was

tested at no less than 15 points.

3. Results and discussion

3.1. Microstructure of the HEA coatings

The XRD spectra of the two HEA coatings before irradiation were shown in Fig. 2. Both coatings had single-phase body-centered cubic (BCC) structures and showed strong (110), weak (220) peaks, and weak (211) peaks in VCrTaW coating. The surface morphology of NbMoTaW and VCrTaW HEA coatings and grain size distribution was shown in Fig. 3, and both coatings were single-phase structures interwoven with sheet nanocrystals, and the grain edges were clear, indicating that the grains nucleation growth was sufficient during the coatings deposition process. For the two coatings before irradiation, about 300 sheet grains along the length direction was calculated and the average grain sizes were 382 ± 91 nm (NbMoTaW coating) and 416 ± 112 nm (VCrTaW coating), respectively. It was worth noting that both materials show good stability after high-dose irradiation, and the grain structure did not change significantly.

The EDS-Mapping results were shown in Fig. 4, the composition of both coatings was evenly distributed. Fig. 5 showed the cross-sectional TEM and selected area electron diffraction (SAED) images taken in [001] zone axis direction of the two coatings (the irradiation dose was 50 dpa), the samples prepared by FIB with a sufficient depth, and the sample included two parts, the coatings and substrate. NbMoTaW and VCrTaW coatings thickness was 3800 nm and 3100 nm, respectively. The SAED results showed that both high-entropy alloy coatings were single-phase BCC structures, the crystal plane spacing of {110} in

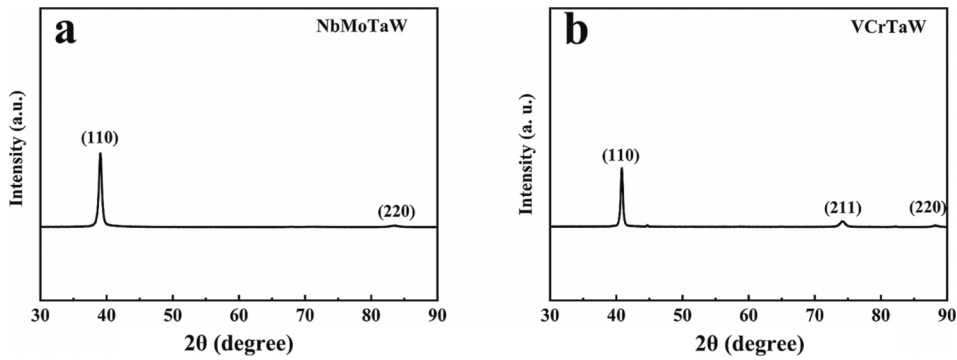


Fig. 2. XRD patterns of the two HEA coatings before irradiation: (a) NbMoTaW coating, (b) VCrTaW coating.

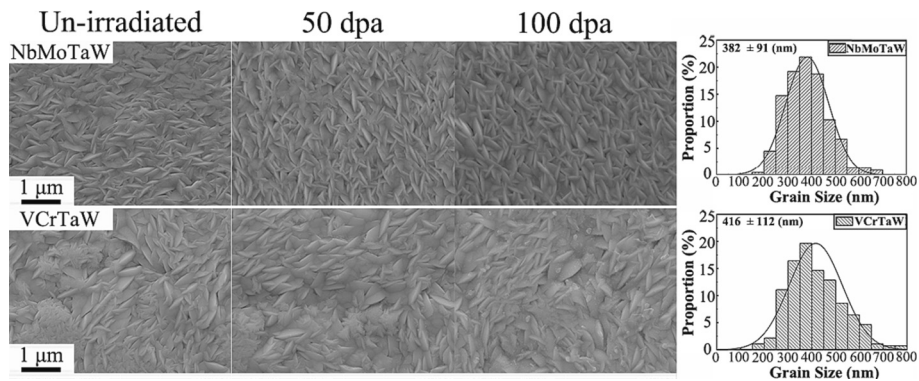


Fig. 3. SEM images of NbMoTaW and VCrTaW coatings before and after irradiation and grain size distribution before irradiation.

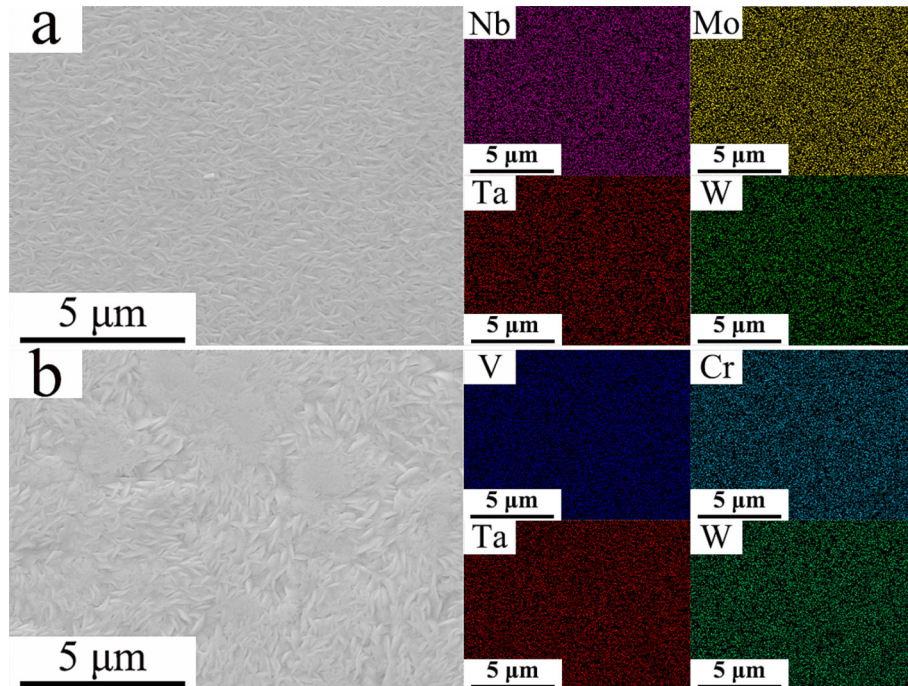


Fig. 4. Elements mappings of the two coatings before irradiation: (a) NbMoTaW coating, (b) VCrTaW coating.

NbMoTaW coating was 1/4.40 nm and the lattice constant $a = 3.214 \text{ \AA}$, crystal plane spacing of {110} in VCrTaW coating was 1/4.30 nm, then the lattice constant $a = 3.289 \text{ \AA}$. Although the ion irradiation depth did not reach the interface between the coatings and the substrate, at the same time of irradiation, the coatings were annealed at 550 °C for 15 h,

and the coatings and substrates were still tightly bonded, without voids and cracks, showing good high-temperature stability.

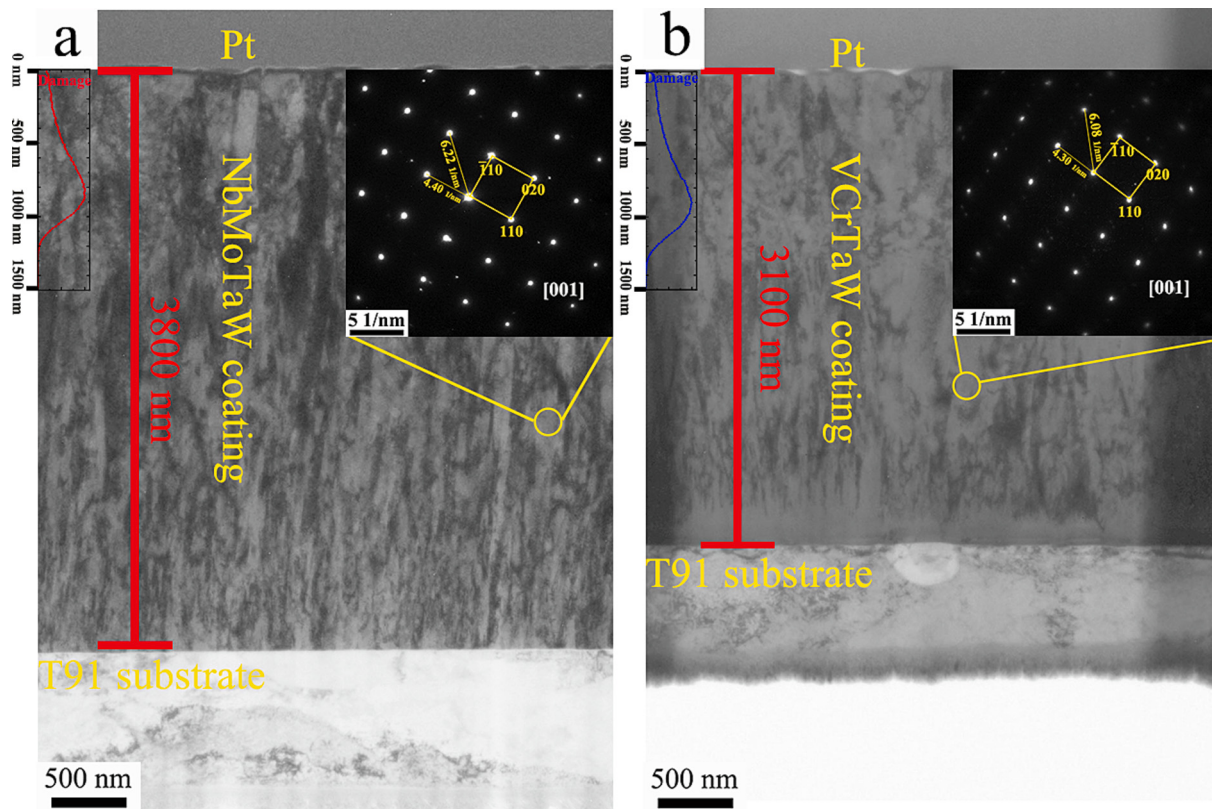


Fig. 5. Cross-sectional TEM and SAED images of two coatings: (a) NbMoTaW coating, (b) VCrTaW coating. The SAED patterns were taken in [001] zone axis direction.

3.2. Dislocation loops

Fig. 6 was the cross-sectional bright-field (BF) TEM images of the dislocation loops in T91 after 50 dpa and 100 dpa irradiation, to exclude the influence of surface effects and gap ions implantation effects on the microstructure [37], dislocation loops with depths in the range of 450 nm - 750 nm were selected for observation. Fig. 6(a) and 6(b) were dislocation loops images observed along different g conditions near the [1-10] zone axis when the peak damage was 50 dpa, the red solid circles were typically visible dislocation loops, and the red dotted circles

indicated that the dislocation loops were not visible. The number of dislocation loops under the $g = 110$ condition was significantly higher than that under the $g = 002$ condition. For BCC materials, the Burgers vectors of irradiation-induced dislocation loops could be $\langle 111 \rangle$ or $\langle 100 \rangle$ [38], according to the $g \cdot b = 0$ invisibility criterion, the proportion of $\langle 100 \rangle$ type dislocation loops was higher. Fig. 6(c) and Fig. 6(d) were dislocation loops images observed in different g conditions near the [001] zone axis when the peak damage was 100 dpa, and the number of dislocation loops visible in the $g = 110$ condition was significantly more than in the $g = 200$ condition, the situation was close to 50 dpa.

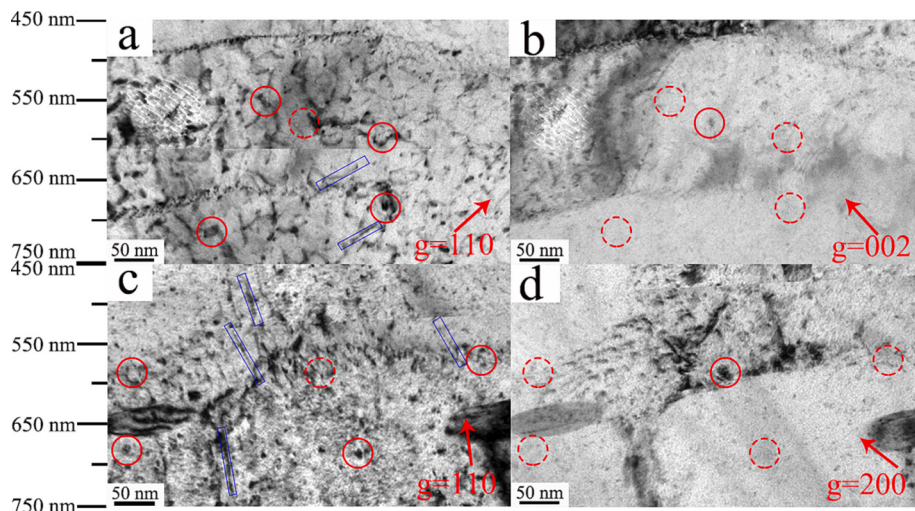


Fig. 6. BF-TEM images of the dislocation loops with T91 after irradiation: (a) 50 dpa, $g = 110$ near the [1-10] zone axis (b) 50 dpa, $g = 002$ near the [1-10] zone axis, (c) 100 dpa, $g = 110$ near the [001] zone axis, (d) 100 dpa, $g = 200$ near the [001] zone axis. The red circles were typical dislocation loops, with solid lines indicating visible and dashed lines indicating invisible. The blue boxes were dislocation lines.

Considering only the case in the $g = 110$ condition, the dislocation loops size was smaller at 100 dpa and the number of dislocation lines (blue boxes area) was higher at 100 dpa compared to 50 dpa.

Fig. 7(a-b) and **7(c-d)** were cross-sectional BF-TEM images of dislocation loops in NbMoTaW and VCrTaW coatings after 50 dpa and 100 dpa irradiation, all images were taken in the condition of $g = 110$ near the [001] zone axis. Due to the depth distribution of ion irradiation damage, the evolution of dislocation loops between the two HEA coatings and T91 under similar dpa was more statistically significant, so the dislocation loops statistical analysis was carried out for the selected depth range of 300 nm – 600 nm for the two HEA coatings. For both NbMoTaW and VCrTaW coatings, the number density of dislocation loops decreased as the peak displacement damage increased from 50 dpa to 100 dpa.

Fig. 8 showed the size and number density statistical results of the dislocation loops in T91 and two HEA coatings with irradiation doses. For T91, the dislocation loops size decreased from 12.8 ± 4.6 nm to 10.2 ± 2.1 nm and the number density decreased from $6.2 \pm 0.9 \times 10^{21}/\text{m}^3$ to $5.9 \pm 1.1 \times 10^{21}/\text{m}^3$ after increasing the irradiation doses from 50 dpa to 100 dpa. Considering the measurement error of the BF-TEM image caused by diffraction contrast, it could suppose that the size of dislocation loops did not change much at the two doses. The phenomenon of dislocation loops in iron-based alloys first growing and then saturating with increasing doses had been reported at different temperatures. Du et al. [39] used neutrons to irradiate 316 stainless steel at 320 °C, the damage reached 67.4 dpa and 125.4 dpa, the dislocation loops size decreased slightly with increasing doses, and the number density did not change much, it was close to the results of this study. Zheng et al. [24] used 1 MeV, Kr²⁺ ions to irradiate T91 with damage doses from 0 to 10 dpa at 470 °C, and the dislocation loops size and number density hardly changed after 4 dpa. At higher temperatures, such as Xie et al. [40] observed that the dislocation loops size was 7.3 ± 1.7 nm and the number density was $1.79 \pm 0.67 \times 10^{21}/\text{m}^3$ after irradiation CLAM steel at 550 °C with a dose of 15 dpa, which was lower than that of this study. Based on the above results, we considered that the higher irradiation temperature enhances the ability of point defect migration and merger, increases the dpa required when the dislocation loops were fully evolved, and after irradiation 50 dpa at 550 °C, the dislocation loops had been saturated, and further increasing the dpa will only increase the probability of the interaction between the dislocation loops and the dislocation lines, resulting in more dislocation loops networking (this part of the dislocation loops accounts for a small proportion of the whole), which had little effect on the dislocation loops size and number density.

Lu et al. [41] prepared a series of single-phase solid-solution alloys, NiFe, NiCoFe, NiCoFeCr and NiCoFeCrMn, and after irradiation to $38 \pm$

5 dpa at 773 K using 3 MeV, Ni²⁺ ions, it was found that the number density of dislocation loops increased and the dislocation loops size decreased with the increase of alloying element species, indicating that the addition of alloying elements could delay the evolution of dislocation loops. Although the chemical components of T91 and the two HEA coatings in this study were not comparable, the number of main alloying elements of the two HEA coatings was more than that of T91, which can delay the evolution of dislocation loops had also been confirmed in this study: with the increase of dpa, the size of the dislocation loops of the two HEA coatings increased, and the number density decreased, indicated that the dislocation loops formed by the migration of the point defects caused by irradiation at 50 dpa did not reach saturation, and with the increase of the dose to 100 dpa, the dislocation loops further absorbed the point defect and the probability of merging between the dislocation loops increased, increased dislocation loops size and the decrease of the number density.

Many key properties of HEAs could be related to lattice mismatch degree (δ) caused by differences in atomic size, resulting in strong local lattice distortions and changes the mobility of different elements [42]. According to the lattice parameters obtained by SAED and the calculation method in Ref. [43], we found that the lattice mismatch degree of NbMoTaW was only 2.34 %, while that of VCrTaW was 6.14 %. Therefore, VCrTaW coating had a higher dislocation loops number density than NbMoTaW coating while the dislocation loops size was not much different, which may be due to the higher lattice mismatch degree resulting in point defect migration range smaller, increasing dislocation loops nucleation sites in VCrTaW coating.

3.3. Irradiation segregation

Fig. 9(a-b) showed the dark-field scanning transmission electron microscopy (DF-STEM) images and EDS line scanning results of the unirradiated and irradiated regions near the grain boundaries of the NbMoTaW and VCrTaW coatings after 100 dpa irradiation. For NbMoTaW coating, the grain boundaries in the unirradiated regions were clear and the irradiated regions were ambiguous, there were obvious depletion phenomena of Ta and W elements at the grain boundary of the unirradiated regions, while the depletion phenomenon of Ta and W elements at the grain boundary disappeared after irradiation, that was, the irradiation led to the migration of Ta and W elements to the grain boundary. For VCrTaW coating, no obvious enrichment and depletion of four elements were found along grain boundaries before and after irradiation.

Zhang et al. [44] prepared NbMoTaW with the same atomic ratio by vacuum arc melting and found that Ta and W elements were depleted at the grain boundary, which was consistent with the results of this study.

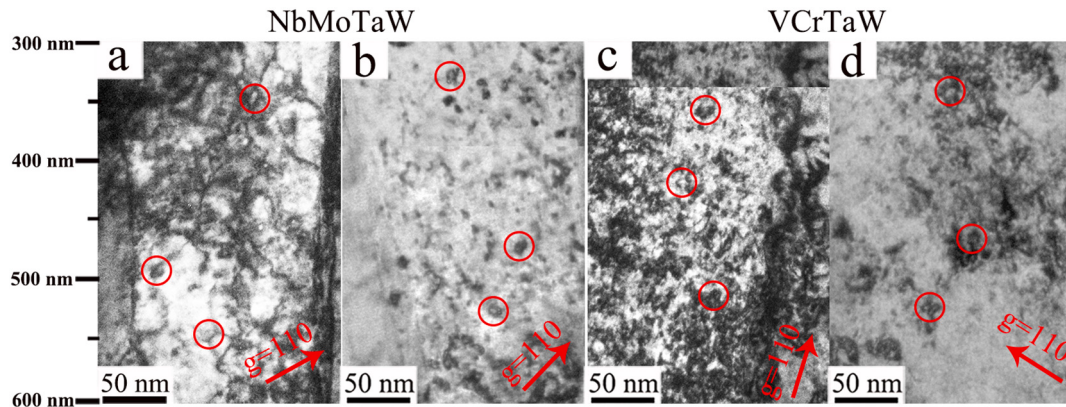


Fig. 7. BF-TEM images of dislocation loops with two HEA coatings after irradiation: (a) NbMoTaW coating, 50 dpa, (b) NbMoTaW coating, 100 dpa, (c) VCrTaW coating, 50 dpa, (d) VCrTaW coating, 100 dpa. The red circles were typical dislocation loops, and all images were taken in the condition of $g = 110$ near the [001] zone axis.

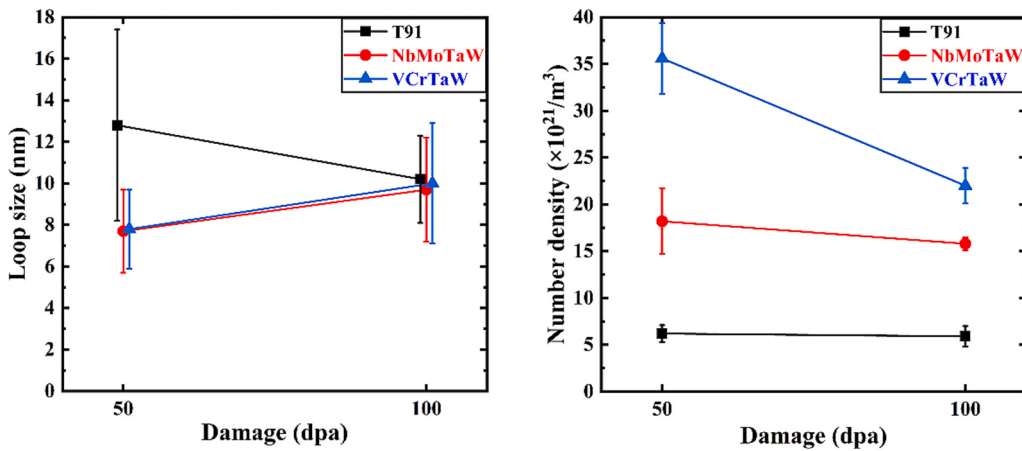


Fig. 8. Statistical results of dislocation loops size and number density after irradiation of T91, NbMoTaW and VCrTaW coatings.

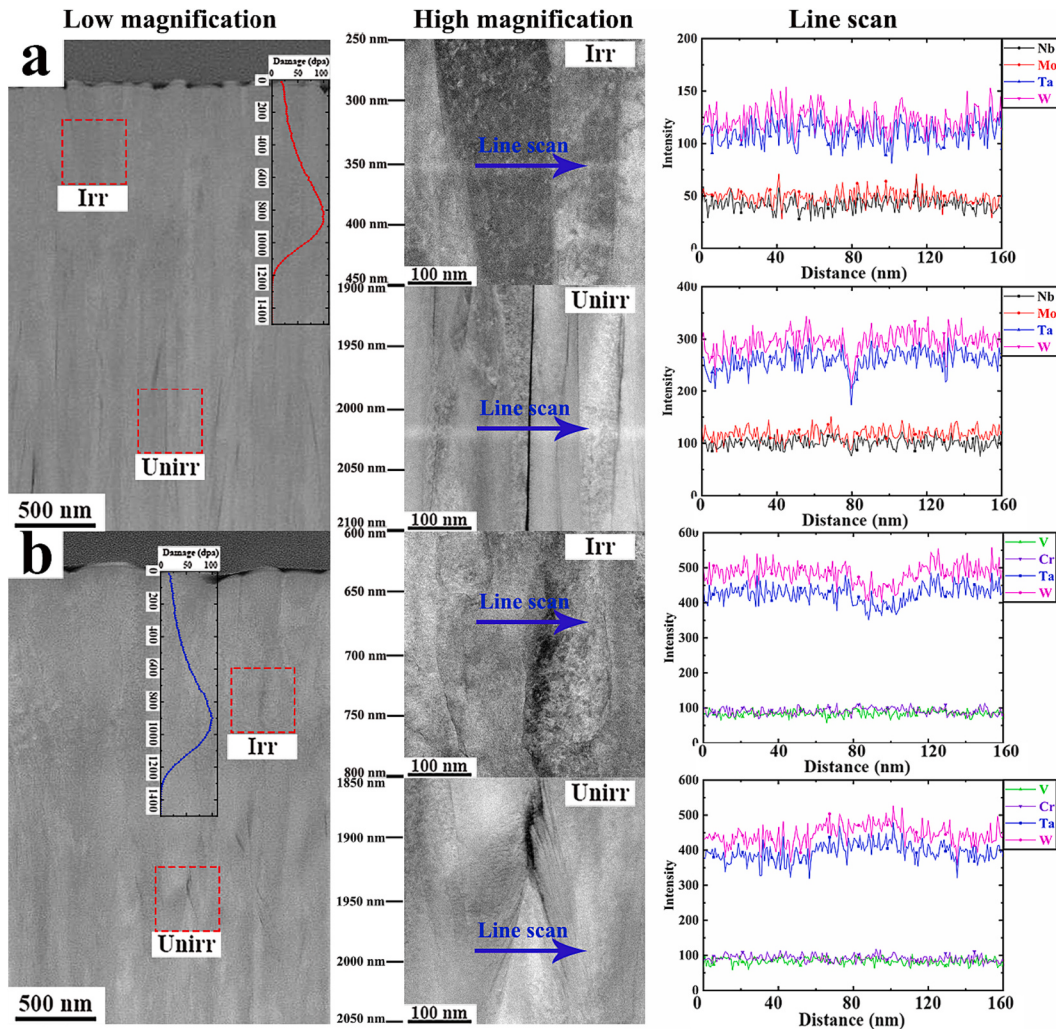


Fig. 9. DF-STEM images and EDS line scanning results near grain boundaries in irradiated and unirradiated regions: (a) NbMoTaW coating, (b) VCrTaW coating.

The reason could be attributed to the greater segregation coefficient of Ta and W [32]. Irradiation-enhanced diffusion could lead to the redistribution of elements within a certain range, especially the segregation of elements near grain boundaries was a common phenomenon [45–47]. There were generally two perspectives on understanding this process [20]: One opinion was the interstitial atom interaction mechanism,

where interstitial atoms produced by irradiation preferentially combine with smaller size atoms to form dumbbell-shaped pairs of interstitial atoms that diverge toward grain boundaries, causing them to enrich at grain boundaries. However, among the four elements of NbMoTaW, the atomic radius was Ta (2.00 Å) > Nb (1.98 Å) > W (1.93 Å) > Mo (1.90 Å) [48]. Therefore, the interstitial atom interactions mechanism seemed

not to be able to explain the migration and enrichment of Ta and W elements to grain boundaries after irradiation of NbMoTaW coating. Another view was the Perks model based on the inverse Kirkendall effect, which argued that the interaction between solute atoms and vacancies caused by irradiation cascade damage was the main cause of irradiation-induced segregation, and solute atoms with lower vacancy exchange rate tend to enrich at grain boundaries [49]. Unfortunately, there was no report on the exchange capacity of solute atoms and vacancies in NbMoTaW coating. Therefore, we speculated that the exchange rate of Ta and W with vacancy may be lower than that of Nb and Mo under irradiation, resulting in the migration of Ta and W elements toward grain boundaries. This phenomenon could also explain the fewer dislocations in NbMoTaW than VCrTaW: The dislocation loops induced by irradiation were mainly interstitial type. After irradiation, Ta and W elements in the NbMoTaW sample migrated to the grain boundaries and left vacancies inside the grains, which annihilated with the interstitial atoms generated by irradiation, thereby reducing the number of interstitial atoms inside the grains and ultimately reduced the number of dislocation loops.

In addition, considering the microstructure heterogeneity and element segregation will greatly reduce the corrosion resistance of the alloy [50,51], and the homogenization of elements near grain boundaries may produce better corrosion resistance in NbMoTaW coating after high-dose irradiation, which is worthy of further study.

3.4. Irradiation hardening

Fig. 10 was the nanoindentation test result, the indenter was greatly affected by the surface at the beginning of pressing into the samples, so the data in the range of 0 nm - 100 nm from the surface was not retained, and the average of the test curves of each sample was obtained Fig. 10

(a). The change of hardness with depth does not correspond to the change of irradiation damage with depth, which was mainly due to the indentation size effect (ISE), and the Nix-Gao model could be used to properly exclude ISE [52], as Eq. (1),

$$H^2 = H_0^2 \left(1 + \frac{h^*}{h} \right) \quad (1)$$

where H was the hardness value at the test depth h , H_0 was the hardness at infinite depth, and h^* was the characteristic parameter related to the type of indenter and the material. Hosemann et al. [53] showed that the nanoindentation test results corresponding to 1/5 of the irradiation depth could reasonably reflect the real sample's hardness, so we selected the data in the range of 100 nm - 250 nm for linear fitting according to Eq. (1) to obtain Fig. 10(b). The intercept obtained by fitting in Fig. 10 (b) was H_0^2 , and Fig. 10(c) was the fitted hardness value by the Nix-Gao model for each sample. $\Delta H (\Delta H = H^{irr} - H^{unirr})$ was the hardening increment before and after irradiation, as shown in Fig. 10(d). It could be seen that the hardening increment of T91 after 50 dpa and 100 dpa irradiation was small, while the hardening of NbMoTaW and VCrTaW coatings was obvious after irradiation. For the two HEA coatings, the hardening increment after 100 dpa irradiation was less than 50 dpa irradiation, indicating that the hardening after 50 dpa was close to saturation. The hardening rate (Hardening rate = 100% × $\Delta H / H^{unirr}$) could better reflect the hardening degree of each material, the specific values were shown in Table 2. The hardening rate of NbMoTaW coating was lower than that of VCrTaW coating at the two doses, indicating that NbMoTaW coating had better irradiation hardening resistance performance.

Irradiation hardening mainly comes from various defects caused by irradiation (observable under TEM, such as dislocation loops, and un-

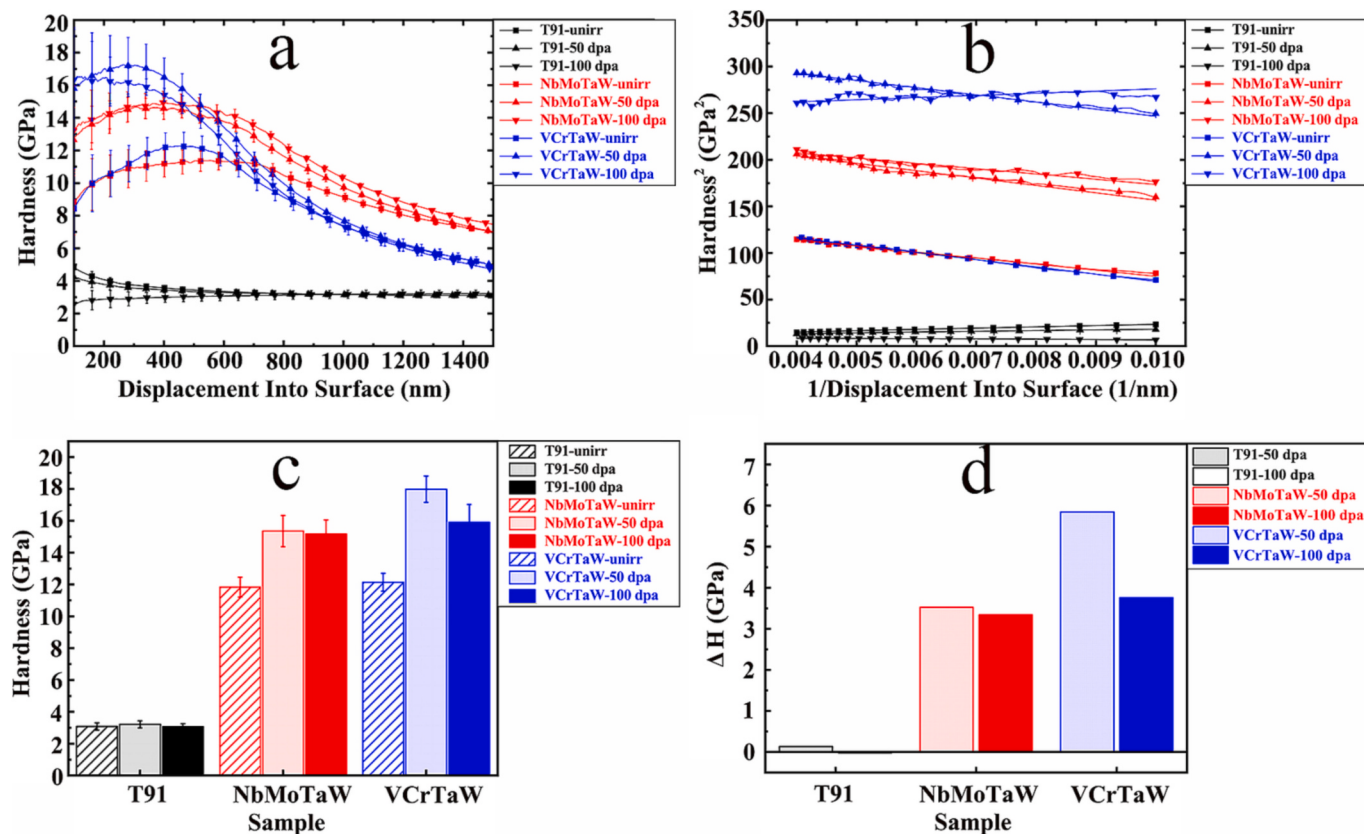


Fig. 10. Nanoindentation test results of T91 and the two HEA coatings before and after irradiation: (a) the average value of the original nanoindentation test data, (b) fitting results of hardness values in the range of 100 nm - 250 nm according to the Nix-Gao model, (c) fitting hardness values before and after irradiation, (d) hardening increment (ΔH).

Table 2

Experimental data of T91 and two HEA coatings.

Sample	Damage (dpa)	Hardness (GPa)	Loops size (nm)	Loops density ($\times 10^{21}/\text{m}^3$)	ΔH (GPa)	ΔH_c (GPa)	Hardening rate
T91	0	3.09 ± 0.23	–	–	–	–	–
	50	3.22 ± 0.22	12.8 ± 4.6	6.2 ± 0.9	0.13	0.69	4.21 %
	100	3.07 ± 0.20	10.2 ± 2.1	5.9 ± 1.1	−0.02	0.60	−0.65 %
NbMoTaW	0	11.83 ± 0.63	–	–	–	–	–
	50	15.36 ± 0.98	7.7 ± 2.0	18.2 ± 3.5	3.52	1.07	29.75 %
	100	15.17 ± 0.89	9.7 ± 2.5	15.8 ± 0.7	3.34	1.36	21.74 %
VCrTaW	0	12.14 ± 0.56	–	–	–	–	–
	50	17.98 ± 0.83	7.8 ± 1.9	35.6 ± 3.8	5.84	1.40	48.11 %
	100	15.90 ± 1.13	10.0 ± 2.9	22.0 ± 1.9	3.76	1.25	30.97 %

observable, such as small-sized vacancies and gap atomic clusters), the influence of dislocation loops on hardening was generally considered to be the main one, and this part of the hardening amount could be evaluated by dispersed barrier hardening (DBH) model. The formula was as follows [54]:

$$\Delta\sigma_y = M\alpha b\sqrt{Nd} \quad (2)$$

$$\mu = \frac{E}{2(1+\nu)} \quad (3)$$

The relationship between hardness and yield stress was formula 4 [55].

$$\Delta H_c \approx 3\Delta\sigma_y \quad (4)$$

M was the Taylor factor 3.06 for BCC alloys, α was barrier strength factor 0.4 for dislocation loops, μ was the shear modulus, which was obtained by Young's modulus E (obtained by nanoindentation test, the values of T91, NbMoTaW coating and VCrTaW coating were 220 GPa, 270 GPa and 240 GPa, respectively) and Poisson's ratio ν (0.3 for all samples) by formula (3) [56]. b was the Burgers vector for gliding dislocations (for alpha iron, $b = 0.248 \text{ nm}$ [57]), N was the density of dislocation loops and d was the diameter of dislocation loops. The ΔH_c calculated from DBH model was shown in Table 2. For the hardness increment of the three materials at different doses, the hardness increment (ΔH_c) generated by the dislocation loops calculated by the DBH model and the hardness increment (ΔH) obtained by fitting according to the Nix-Gao model coincide in trend, but the numerical difference was large, indicating that the dislocation loops was not the only source of hardening after high-dose irradiation.

For T91, the hardening increment obtained by the nanoindentation test (ΔH) was smaller than the hardening increment generated by the dislocation loops calculated by the DBH model (ΔH_c). Li et al. [58] used Fe²⁺ irradiation CLAM steel to different damage doses at 300 °C and 550 °C, respectively, and found that at 550 °C, hardening did not increase linearly with the increase of irradiation damage doses, and even when the irradiation damage dose was higher than 0.79 dpa, it showed irradiation softening, and the softening could be attributed to the recovery of defects under high-temperature irradiation. It was shown that for T91, the irradiation process occurred simultaneously with hardening and softening, and the final increment of hardening depends on the competitive mechanism between the hardening and softening, which may explain the almost no significant hardening of T91 at both doses in this study.

For the two HEA coatings, the hardness of VCrTaW coating was higher than NbMoTaW coating before and after irradiation, which may be related to the higher lattice mismatch degree of VCrTaW [43]. The hardening increment obtained by the nanoindentation test (ΔH) was much higher than the hardening increment caused by the dislocation loops calculated by the DBH model (ΔH_c), indicating that the influence of the dislocation loops on hardening was only partial. Molecular dynamics simulations showed that the vacancy formation energy of W-V-Cr and W-Ta-V alloys was lower than that of pure W, resulting in a higher equilibrium vacancy concentration [59], and due to small

vacancies were difficult to observe by TEM, but their contribution to hardening couldn't be ignored.

At the same time, the hardening increment decreased with the increase in doses. The WTaVCr samples prepared by El-Atwani et al. [23] with a hardness of about 14 GPa before irradiation, and after irradiation by Kr²⁺ at 1073 K at 8 dpa, the irradiation hardening was almost negligible. However, in AlCrFeMoTi HEA coating, after Au ion irradiation at room temperature, the hardness increment increases linearly with the damage doses, which was 8.32 GPa before irradiation, and 15.02 GPa after irradiation at 90 dpa, and the hardening rate was as high as 80.5 % [60]. Similarly, FeNiMnCr was irradiated at 300 °C and 450 °C at different doses (0.2 dpa, 2 dpa, 20 dpa), and it was found that the hardening increment increased with the increase of doses, and the hardening increment could reach more than 4 GPa after 20 dpa irradiation [61]. The above research results showed that the irradiation hardening of HEAs was affected by both irradiation temperature and irradiation damage doses. The high temperature will reduce the irradiation hardening while increasing the damage doses will increase the irradiation hardening, which was consistent with the variation trend of irradiation hardening and softening with temperature and doses proposed by Li et al. [58]. This study was only conducted at 550 °C, the possible reason why the hardening increment after 100 dpa irradiation was lower than 50 dpa was that compared with 50 dpa irradiation at 550 °C, the softening caused by point defect recovery after 100 dpa irradiation was greater than the hardening caused by dislocation loops.

4. Conclusions

In this study, NbMoTaW and VCrTaW HEA coatings were first deposited on the T91 substrate and then irradiated to 50 dpa and 100 dpa by 2.7 MeV Si²⁺ at 550 °C to evaluate the irradiation resistance of the HEA coatings. The results were as follows:

1. The two HEA coatings had similar grain morphology and size distribution and remain stable after irradiation. After irradiation, they had good thermodynamic stability with the T91 substrate under the action of annealing.
2. A large number of dislocation loops were generated after the irradiation of T91 and HEA coatings. With the increase of irradiation doses, the size of dislocation loops in HEA coatings increased and the number density decreased, the number density in VCrTaW was higher than that in NbMoTaW. Compared to T91 substrate, the HEA coatings had better irradiation resistance.
3. The Ta and W elements near the grain boundary of NbMoTaW were depleted before irradiation and homogenized after irradiation. All of the elements near grain boundaries in VCrTaW were stable after irradiation.
4. The irradiation hardening of T91 was not obvious at two irradiation doses. The two kinds of HEA coatings hardening obviously after irradiation and after 50 dpa was higher than 100 dpa irradiation. The hardening increment of dislocation loops calculated by the DBH model was not in good agreement with the hardening increment obtained by the nanoindentation test. The main reason was that

- hardening and softening exist simultaneously under high-temperature irradiation, and the final hardening depends on the competition between them.
5. Considering defects density and hardening rate, the irradiation resistance of NbMoTaW was preliminarily better than that of VCrTaW.

CRediT authorship contribution statement

Hongtai Luo: Validation, Investigation, Writing – original draft, Writing – review & editing. **Bin Long:** Conceptualization, Methodology, Supervision, Resources, Project administration, Funding acquisition. **Shenghui Lu:** Investigation, Writing – review & editing. **Liping Guo:** Conceptualization, Methodology, Supervision, Resources, Project administration, Funding acquisition. **Fengfeng Luo:** Investigation, Writing – review & editing, Project administration, Funding acquisition. **Wenbin Lin:** Investigation. **Junjie Cao:** Investigation. **Zepeng Yin:** Investigation. **Peili Zhao:** Investigation.

Declaration of competing interest

The authors declare that they have no known competing financial interests or personal relationships that could have appeared to influence the work reported in this paper.

Data availability

Data will be made available on request.

Acknowledgments

This study was supported by the National Natural Science Foundation of China (Grant Nos. U2067219, 11975170 and 12105123).

Appendix A. Supplementary data

Supplementary data to this article can be found online at <https://doi.org/10.1016/j.surfcoat.2023.130019>.

References

- [1] G. Bandini, P. Meloni, M. Polidori, Thermal-hydraulics analyses of ELSY lead fast reactor with open square core option, *Nucl. Eng. Des.* 241 (2011) 1165–1171, <https://doi.org/10.1016/j.nucengdes.2010.04.034>.
- [2] T. Okawa, H. Sekimoto, Design study on Pb-208 cooled CANDLE burning reactors toward practical application for future nuclear energy source, *Prog. Nucl. Energy* 53 (2011) 886–890, <https://doi.org/10.1016/j.pnucene.2011.05.015>.
- [3] F. Sar, S. Mhiaoui, J.G. Gasser, Thermal conductivity of liquid lead-bismuth alloys, possible coolants for fourth generation spallation nuclear reactors, *J. Non-Cryst. Solids* 353 (2007) 3622–3627, <https://doi.org/10.1016/j.jnoncrysol.2007.05.171>.
- [4] X. Gong, M.P. Short, T. Auger, E. Charalampopoulou, K. Lambrinou, Environmental degradation of structural materials in liquid lead- and lead-bismuth eutectic-cooled reactors, *Prog. Mater. Sci.* 126 (2022), <https://doi.org/10.1016/j.pmatsci.2022.100920>.
- [5] R. Yu, L. Gu, X. Sheng, J. Li, Y. Zhu, L. Zhang, W. Jiang, Review of fuel assembly design in lead-based fast reactors and research progress in fuel assembly of China initiative accelerator driven system, *Int. J. Energy Res.* 45 (2021) 11552–11563, <https://doi.org/10.1002/er.6569>.
- [6] S.J. Tian, Z.Z. Jiang, L. Luo, Oxidation behavior of T91 steel in flowing oxygen-containing lead-bismuth eutectic at 500 °C, *Mater. Corros.* 67 (2016) 1274–1285, <https://doi.org/10.1002/maco.201609075>.
- [7] X. Gong, R. Li, M. Sun, Q. Ren, T. Liu, M.P. Short, Opportunities for the LWR ATF materials development program to contribute to the LBE-cooled ADS materials qualification program, *J. Nucl. Mater.* 482 (2016) 218–228, <https://doi.org/10.1016/j.jnucmat.2016.10.012>.
- [8] Z. Ma, T. Shen, T. Zhou, Z. Wang, Performance of the new ferritic/martensitic steel SIMP against liquid lead-bismuth eutectic corrosion: comparison with T91 and 316L steels, *Mater. Corros.* (2022), <https://doi.org/10.1002/maco.202213372>.
- [9] G. Müller, G. Schumacher, F. Zimmermann, Investigation on oxygen controlled liquid lead corrosion of surface treated steels, *J. Nucl. Mater.* 278 (2000) 85–95, [https://doi.org/10.1016/S0022-3115\(99\)00211-1](https://doi.org/10.1016/S0022-3115(99)00211-1).
- [10] J. Zhang, N. Li, Y. Chen, A.E. Rusanov, Corrosion behaviors of US steels in flowing lead-bismuth eutectic (LBE), *J. Nucl. Mater.* 336 (2005) 1–10, <https://doi.org/10.1016/j.jnucmat.2004.08.002>.
- [11] E.I. Yefimov, Nuclear engineering and design use of lead-bismuth coolant in nuclear reactors and, *Nucl. Eng. Des.* 173 (1997) 207–217.
- [12] J.G. Marques, Evolution of nuclear fission reactors: third generation and beyond, *Energy Convers. Manag.* 51 (2010) 1774–1780, <https://doi.org/10.1016/j.enconman.2009.12.043>.
- [13] D. Sapundjiev, S. Van Dyck, W. Bogaerts, Liquid metal corrosion of T91 and A316L materials in Pb-Bi eutectic at temperatures 400–600 °C, *Corros. Sci.* 48 (2006) 577–594, <https://doi.org/10.1016/j.corsci.2005.04.001>.
- [14] A. Alemberti, J. Carlsson, E. Malambo, A. Orden, D. Struwe, P. Agostini, S. Monti, European lead fast reactor - ELSY, *Nucl. Eng. Des.* 241 (2011) 3470–3480, <https://doi.org/10.1016/j.nucengdes.2011.03.029>.
- [15] S.J. Zinkle, J.T. Busby, Structural materials for fission & fusion energy, *Mater. Today* 12 (2009) 12–19, [https://doi.org/10.1016/S1369-7021\(09\)70294-9](https://doi.org/10.1016/S1369-7021(09)70294-9).
- [16] J.W. Yeh, S.K. Chen, S.J. Lin, J.Y. Gan, T.S. Chin, T.T. Shun, C.H. Tsau, S.Y. Chang, Nanostructured high-entropy alloys with multiple principal elements: novel alloy design concepts and outcomes, *Adv. Eng. Mater.* 6 (2004) 299–303, <https://doi.org/10.1002/adem.200300567>.
- [17] F. Körmann, A.V. Ruban, M.H.F. Sluiter, Long-ranged interactions in bcc NbMoTaW high-entropy alloys, *Mater. Res. Lett.* 5 (2017) 35–40, <https://doi.org/10.1080/21663831.2016.1198837>.
- [18] J. Chen, X. Zhou, W. Wang, B. Liu, Y. Lv, W. Yang, D. Xu, Y. Liu, A review on fundamental of high entropy alloys with promising high-temperature properties, *J. Alloys Compd.* 760 (2018) 15–30, <https://doi.org/10.1016/j.jallcom.2018.05.067>.
- [19] Z. Li, S. Zhao, R.O. Ritchie, M.A. Meyers, Mechanical properties of high-entropy alloys with emphasis on face-centered cubic alloys, *Prog. Mater. Sci.* 102 (2019) 296–345, <https://doi.org/10.1016/j.pmatsci.2018.12.003>.
- [20] Z. Cheng, J. Sun, X. Gao, Y. Wang, J. Cui, T. Wang, H. Chang, Irradiation effects in high-entropy alloys and their applications, *J. Alloys Compd.* 930 (2023) 166768, <https://doi.org/10.1016/j.jallcom.2022.166768>.
- [21] Y. Shi, B. Yang, P.K. Liaw, Corrosion-resistant high-entropy alloys: a review, *Metals (Basel)* 7 (2017) 1–18, <https://doi.org/10.3390/met7020043>.
- [22] M.H. Tsai, J.W. Yeh, High-entropy alloys: a critical review, *Mater. Res. Lett.* 2 (2014) 107–123, <https://doi.org/10.1080/21663831.2014.912690>.
- [23] O. El-Atwani, N. Li, M. Li, A. Devaraj, J.K.S. Baldwin, M.M. Schneider, D. Sobieraj, J.S. Wróbel, D. Nguyen-Manh, S.A. Maloy, E. Martinez, Outstanding radiation resistance of tungsten-based high-entropy alloys, *Sci. Adv.* 5 (2019) 1–10, <https://doi.org/10.1126/sciadv.aav2002>.
- [24] C. Zheng, D. Kaoumi, Dislocation loop evolution in F/M steel T91 under in-situ ion irradiation: influence of the presence of initial dislocations, *J. Nucl. Mater.* 540 (2020), <https://doi.org/10.1016/j.jnucmat.2020.152363>.
- [25] L.J. Santodonato, Y. Zhang, M. Feygenson, C.M. Parish, M.C. Gao, R.J.K. Weber, J. C. Neufeind, Z. Tang, P.K. Liaw, Deviation from high-entropy configurations in the atomic distributions of a multi-principal-element alloy, *Nat. Commun.* 6 (2015), <https://doi.org/10.1038/ncomms6964>.
- [26] J. Yang, K. Shi, W. Zhang, Q. Chen, Z. Ning, C. Zhu, J. Liao, Y. Yang, N. Liu, J. Yang, A novel AlCrFeMoTi high-entropy alloy coating with a high corrosion-resistance in lead-bismuth eutectic alloy, *Corros. Sci.* 187 (2021), <https://doi.org/10.1016/j.corsci.2021.109524>.
- [27] L. La, L. Wang, F. Liang, J. Zhang, G. Liang, Z. Wang, L. Qin, High-temperature oxidation and tribological behaviors of WTaVCr alloy coating prepared by double glow plasma surface alloying technology, *Surf. Coat. Technol.* 464 (2023), <https://doi.org/10.1016/j.surfcoat.2023.129429>.
- [28] O.N. Senkov, G.B. Wilks, J.M. Scott, D.B. Miracle, Mechanical properties of Nb25Mo25Ta 25W25 and V20Nb20Mo 20Ta20W20 refractory high entropy alloys, *Intermetallics* 19 (2011) 698–706, <https://doi.org/10.1016/j.intermet.2011.01.004>.
- [29] T. Shi, P.H. Lei, X. Yan, J. Li, Y. Di Zhou, Y.P. Wang, Z.X. Su, Y.K. Dou, X.F. He, D. Yun, W. Yang, C.Y. Lu, Current development of body-centered cubic high-entropy alloys for nuclear applications, *Tungsten*. 3 (2021) 197–217, <https://doi.org/10.1007/s42864-021-00086-6>.
- [30] R.G. Ballinger, J. Lim, An overview of corrosion issues for the design and operation of high-temperature lead- and lead-bismuth - cooled reactor systems, *Nucl. Technol.* 147 (2004) 418–435, <https://doi.org/10.13182/NT04-A3540>.
- [31] L. Qi, D.C. Chrzan, Tuning ideal tensile strengths and intrinsic ductility of bcc refractory alloys, *Phys. Rev. Lett.* 112 (2014) 1–5, <https://doi.org/10.1103/PhysRevLett.112.115503>.
- [32] O.N. Senkov, G.B. Wilks, D.B. Miracle, C.P. Chuang, P.K. Liaw, Refractory high-entropy alloys, *Intermetallics*. 18 (2010) 1758–1765, <https://doi.org/10.1016/j.intermet.2010.05.014>.
- [33] H. Dong, Z. Ye, P. Wang, D. Li, Y. Zhang, Y. Li, Effect of cold rolling on the oxidation resistance of T91 steel in oxygen-saturated stagnant liquid lead-bismuth eutectic at 450 °C and 550 °C, *J. Nucl. Mater.* 476 (2016) 213–217, <https://doi.org/10.1016/j.jnucmat.2016.04.046>.
- [34] Y. Chen, L. Guo, Y. Long, Z. Xie, H. Luo, W. Lin, A Establishment of multi-beam irradiation facility at Wuhan University, *Nucl. Inst. Methods Phys. Res. A* 1040 (2022) 167202, <https://doi.org/10.1016/j.nima.2022.167202>.
- [35] G.S. Was, The displacement of atoms, in: G.S. Was (Ed.), *Fundamentals of Radiation Materials Science*, NY, New York, 2007.
- [36] T. Sato, Y. Aizawa, H. Matsumoto, M. Kiyohara, C. Kamiya, F. von Cube, Low damage lamella preparation of metallic materials by FIB processing with low acceleration voltage and a low incident angle Ar ion milling finish, *J. Microsc.* 279 (2020) 234–241, <https://doi.org/10.1111/jmi.12878>.

- [37] S.J. Zinkle, L.L. Snead, Opportunities and limitations for ion beams in radiation effects studies: bridging critical gaps between charged particle and neutron irradiations, *Scr. Mater.* 143 (2018) 154–160, <https://doi.org/10.1016/j.scriptamat.2017.06.041>.
- [38] H. Xu, R.E. Stoller, Y.N. Osetsky, D. Terentyev, Solving the puzzle of 100 interstitial loop formation in bcc Iron, *Phys. Rev. Lett.* 110 (2013) 1–5, <https://doi.org/10.1103/PhysRevLett.110.265503>.
- [39] D. Du, K. Sun, G.S. Was, Materials Characterization IASCC of Neutron Irradiated 316 Stainless Steel to 125 Dpa, 173, 2021.
- [40] Z. Xie, L. Guo, Y. Chen, Y. Long, F. Li, H. Luo, W. Lin, J. Cao, Q. Huang, S. Mo, Y. Wen, Effect of Helium and Its Synergism With Displacement Damage on Microstructure of CLAM Steel Investigated by Single, Sequential and Simultaneous Fe and He Ion Irradiations 568, 2022.
- [41] C. Lu, T. Yang, K. Jin, N. Gao, P. Xiu, Y. Zhang, F. Gao, H. Bei, W.J. Weber, K. Sun, Y. Dong, L. Wang, Radiation-induced segregation on defect clusters in single-phase concentrated solid-solution alloys, *Acta Mater.* 127 (2017) 98–107, <https://doi.org/10.1016/j.actamat.2017.01.019>.
- [42] G. Wei, J. Byggmästar, J. Cui, K. Nordlund, J. Ren, F. Djurabekova, Effects of lattice and mass mismatch on primary radiation damage in W-Ta and W-Mo binary alloys, *J. Nucl. Mater.* 583 (2023) 154534, <https://doi.org/10.1016/j.jnucmat.2023.154534>.
- [43] B. Yin, F. Maresca, W.A. Curtin, Vanadium is an optimal element for strengthening in both fcc and bcc high-entropy alloys, *Acta Mater.* 188 (2020) 486–491, <https://doi.org/10.1016/j.actamat.2020.01.062>.
- [44] E. Zhang, Y. Tang, M. Wen, A. Obaid, I. Roslyakova, L. Zhang, On phase stability of Mo-Nb-Ta-W refractory high entropy alloys, *Int. J. Refract. Met. Hard Mater.* 103 (2022), <https://doi.org/10.1016/j.ijrmhm.2022.105780>.
- [45] Q. Chen, R. Hu, S. Jin, F. Xue, G. Sha, Irradiation-induced segregation/desegregation at grain boundaries of a ferritic Fe-Mn-Si steel, *Acta Mater.* 220 (2021), <https://doi.org/10.1016/j.actamat.2021.117297>.
- [46] N.A.P.K. Kumar, C. Li, K.J. Leonard, H. Bei, S.J. Zinkle, Microstructural stability and mechanical behavior of FeNiMnCr high entropy alloy under ion irradiation, *Acta Mater.* 113 (2016) 230–244, <https://doi.org/10.1016/j.actamat.2016.05.007>.
- [47] T. Yang, S. Xia, W. Guo, R. Hu, J.D. Poplawsky, G. Sha, Y. Fang, Z. Yan, C. Wang, C. Li, Y. Zhang, S.J. Zinkle, Y. Wang, Effects of temperature on the irradiation responses of Al_{0.1}CoCrFeNi high entropy alloy, *Scr. Mater.* 144 (2018) 31–35, <https://doi.org/10.1016/j.scriptamat.2017.09.025>.
- [48] E. Clementi, D.L. Raimondi, W.P. Reinhardt, Atomic screening constants from SCF functions. II. Atoms with 37 to 86 electrons, *J. Chem. Phys.* 47 (1967) 1300–1307, <https://doi.org/10.1063/1.1712084>.
- [49] Y. Isobe, N. Shigenaka, T. Hashimoto, K. Nakata, M. Kodama, K. Fukuya, K. Asano, Segregation behavior induced by various particle irradiations in austenitic stainless steels, *J. Nucl. Sci. Technol.* 36 (1999) 282–287, <https://doi.org/10.1080/18811248.1999.9726209>.
- [50] K.S. Bal, A. Sadhu, J. Dutta Majumdar, A. Roy Choudhury, Study of melting efficiency, micro-segregation, and corrosion resistance of ytterbium fiber laser welded Hastelloy C-276 sheet in pulsed wave mode, *Adv. Mater. Process. Technol.* 5 (2019) 568–581, <https://doi.org/10.1080/2374068X.2019.1636190>.
- [51] Q. Fan, C. Chen, C. Fan, Z. Liu, X. Cai, S. Lin, C. Yang, Ultrasonic induces grain refinement in gas tungsten arc cladding AlCoCrFeNi high-entropy alloy coatings, *Mater. Sci. Eng. A* 821 (2021), <https://doi.org/10.1016/j.msea.2021.141607>.
- [52] W.D. Nix, H. Gao, Indentation size effects in crystalline materials: a law for strain gradient plasticity, *J. Mech. Phys. Solids* 46 (1998) 411–425, [https://doi.org/10.1016/S0022-5096\(97\)00086-0](https://doi.org/10.1016/S0022-5096(97)00086-0).
- [53] P. Hosemann, D. Kiener, Y. Wang, S.A. Maloy, Issues to consider using nanoindentation on shallow ion beam irradiated materials, *J. Nucl. Mater.* 425 (2012) 136–139, <https://doi.org/10.1016/j.jnucmat.2011.11.070>.
- [54] S.J. Zinkle, Y. Matsukawa, Observation and analysis of defect cluster production and interactions with dislocations, *J. Nucl. Mater.* 329–333 (2004) 88–96, <https://doi.org/10.1016/j.jnucmat.2004.04.298>.
- [55] J.T. Busby, M.C. Hash, G.S. Was, The relationship between hardness and yield stress in irradiated austenitic and ferritic steels, *J. Nucl. Mater.* 336 (2005) 267–278, <https://doi.org/10.1016/j.jnucmat.2004.09.024>.
- [56] X. Yu, J. Zhou, H. Liang, Z. Jiang, L. Wu, Mechanical metamaterials associated with stiffness, rigidity and compressibility: a brief review, *Prog. Mater. Sci.* 94 (2018) 114–173, <https://doi.org/10.1016/j.pmatsci.2017.12.003>.
- [57] P. Song, D. Morrall, Z. Zhang, K. Yabuuchi, A. Kimura, Radiation response of ODS ferritic steels with different oxide particles under ion-irradiation at 550 °C, *J. Nucl. Mater.* 502 (2018) 76–85, <https://doi.org/10.1016/j.jnucmat.2018.02.007>.
- [58] Q. Li, Y. Shen, X. Huang, Z. Xu, J. Zhu, Irradiation-induced hardening and softening of CLAM steel under Fe ion irradiation, *Met. Mater. Int.* 23 (2017) 1106–1111, <https://doi.org/10.1007/s12540-017-7156-0>.
- [59] H. Figiel, O. Zogal, V. Yartys, Atomistic simulations of enhanced irradiation resistance and defect properties in body-centered cubic W-V-Cr and W-Ta-V alloys, *J. Alloys Compd.* 404–406 (2005) 1, <https://doi.org/10.1016/j.jallcom.2005.05.002>.
- [60] J. Yang, K. Shi, Q. Chen, W. Zhang, C. Zhu, Z. Ning, J. Liao, Y. Yang, N. Liu, J. Yang, Effect of au-ion irradiation on the surface morphology, microstructure and mechanical properties of amorphous AlCrFeMoTi HEA coating, *Surf. Coat. Technol.* 418 (2021) 127252, <https://doi.org/10.1016/j.surfcoat.2021.127252>.
- [61] A. Fernández-Caballero, E. Bousser, S.M. Shubeita, P.T. Wady, Y. Gu, R. Krishna, M.J. Gorley, D. Nguyen-Manh, P.M. Mummary, E.J. Pickering, High-dose ion irradiation damage in Fe28Ni28Mn26Cr18 characterised by TEM and depth-sensing nanoindentation, *Nucl. Mater. Energy.* 28 (2021), <https://doi.org/10.1016/j.nme.2021.101028>.